

Kohn-Sham accuracy from orbital-free density functional theory via Δ -machine learning

Shashikant Kumar,¹ Xin Jing,^{1,2} John E. Pask,³ Andrew J. Medford,¹ and Phanish Suryanarayana^{1,2}

¹*College of Engineering, Georgia Institute of Technology, Atlanta, GA 30332, USA*

²*College of Computing, Georgia Institute of Technology, Atlanta, GA 30332, USA*

³*Physics Division, Lawrence Livermore National Laboratory, Livermore, CA 94550, USA*

(*Email: phanish.suryanarayana@ce.gatech.edu)

(Dated: 11 October 2023)

We present a Δ -machine learning model for obtaining Kohn-Sham accuracy from orbital-free density functional theory (DFT) calculations. In particular, we employ a machine learned force field (MLFF) scheme based on the kernel method to capture the difference between Kohn-Sham and orbital-free DFT energies/forces. We implement this model in the context of on-the-fly molecular dynamics simulations, and study its accuracy, performance, and sensitivity to parameters for representative systems. We find that the formalism not only improves the accuracy of Thomas-Fermi-von Weizsäcker (TFW) orbital-free energies and forces by more than two orders of magnitude, but is also more accurate than MLFFs based solely on Kohn-Sham DFT, while being more efficient and less sensitive to model parameters. We apply the framework to study the structure of molten $\text{Al}_{0.88}\text{Si}_{0.12}$, the results suggesting no aggregation of Si atoms, in agreement with a previous Kohn-Sham study performed at an order of magnitude smaller length and time scales.

I. INTRODUCTION

Kohn-Sham density functional theory (DFT)^{1,2} is a widely used ab initio method that has a high accuracy to cost ratio relative to other such first principles methods. However, while less expensive than wavefunction-based methods, Kohn-Sham calculations are still associated with significant computational cost. In particular, they scale cubically with the number of atoms/electrons in the system, a consequence of the orthonormality constraint on the Kohn-Sham orbitals, which restricts the length and time scales accessible to such a rigorous quantum mechanical investigation. This bottleneck is particularly severe in molecular dynamics (MD) simulations, where the Kohn-Sham equations may need to be solved thousands or even hundreds of thousands of times to reach time scales relevant to the phenomena of interest³.

Orbital-free DFT⁴ represents a simplified version of Kohn-Sham DFT in which the orbital-dependent non-interacting kinetic energy functional is replaced by an explicit functional of the electron density. In so doing, the orbitals are removed from the formalism, thereby reducing the problem to the calculation of the electron density alone, in the spirit of the Hohenberg-Kohn theorem². This can also be interpreted as replacing the fictitious system of non-interacting fermions with a fictitious system of non-interacting bosons^{5,6}. The absence of orbitals in orbital-free DFT allows for linear scaling with system size, thereby circumventing the cubic scaling bottleneck inherent in Kohn-Sham DFT. However, an exact kinetic energy functional in terms of the density is currently unknown. Since the pioneering work of Thomas⁷, Fermi⁸, and von Weizsäcker⁹, resulting in the Thomas-Fermi-von Weizsäcker (TFW) functional, the lack of universality has motivated the development of a number of semilocal¹⁰⁻¹⁵, nonlocal¹⁶⁻³¹, and machine learned³²⁻⁴⁰ kinetic energy functionals. However, while advances have been significant, kinetic energy functionals remain limited in accuracy and transferability, particularly for complex systems with significant

inhomogeneity in bonding. Furthermore, the lack of orbitals prevents the use of state-of-the-art pseudopotentials that are available for Kohn-Sham DFT calculations, which further limits the accuracy of orbital-free DFT. Consequently, orbital-free DFT has been less widely used than Kohn-Sham DFT in practice.

Δ -machine learning represents a powerful method for learning the difference in quantities that can be computed from different levels of theory. The effectiveness of such a strategy relies on the qualitative features in the quantities of interest being captured by the lower level of theory, whereby the differences in the quantities between the two theories are smoother and typically more localized than the quantities (obtained from the higher level of theory) themselves. Δ -machine learning has already proven useful in a number of different schemes, including the development of machine learned force fields (MLFFs)⁴¹⁻⁴³ for the difference in energies and/or forces from the following lower level to higher level theories: Kohn-Sham DFT to coupled cluster⁴⁴⁻⁴⁷, Hartree-Fock to coupled cluster⁴⁸⁻⁵⁰, Kohn-Sham DFT to random phase approximation for the correlation energy^{51,52}, and force fields to coupled cluster⁵³⁻⁵⁵. However, the use of such a technique for learning the difference between orbital-free and Kohn-Sham DFT has not been studied heretofore.

In this work, we present a Δ -machine learning scheme for obtaining Kohn-Sham accuracy from orbital-free DFT calculations. In particular, we model the difference in Kohn-Sham and orbital-free DFT energies/forces using a kernel method based MLFF scheme. We implement this model within the context of on-the-fly MD simulations, and study its accuracy, performance, and sensitivity to parameters for representative systems. We find that the formalism not only improves the accuracy of TFW orbital-free DFT energies and forces by more than two orders of magnitude, but is also more accurate than MLFFs developed directly for Kohn-Sham DFT, while being more efficient and less sensitive to the model parameters. We apply the framework to study the possibility of Si aggregation in molten $\text{Al}_{0.88}\text{Si}_{0.12}$.

The remainder of the manuscript is organized as follows. In Section II, we discuss the formulation for the Δ -machine learning model between orbital-free and Kohn-Sham DFT. Next, we study the scheme's accuracy, performance, and sensitivity to model parameters in Section III, where we also apply it to study the structure of molten $\text{Al}_{0.88}\text{Si}_{0.12}$. Finally, we provide concluding remarks in Section IV.

II. FORMULATION

A. Δ -machine learning model

The error in the energy computed by orbital-free DFT can be defined as:

$$E_{\Delta} = E_{\text{KS}} - E_{\text{OF}}, \quad (1)$$

where E_{KS} and E_{OF} are the Kohn-Sham and orbital-free electronic ground state energies, respectively. The dependence of these energies on the atomic positions has been suppressed for notational simplicity, a strategy adopted henceforth for all other such quantities. Since the ground state electron density in orbital-free DFT is *close* to Kohn-Sham DFT⁵⁶, and the electrostatics have the same formalism in both orbital-free and Kohn-Sham DFT, E_{Δ} is largely free from long-range effects, and can therefore be assumed to depend on only the local environment. This makes E_{Δ} particularly well suited for machine learning, as exploited in the MLFF model discussed below.

Given any atomic configuration/structure, we assume that the error in the orbital-free DFT energy can be decomposed as⁵⁷:

$$E_{\Delta} = \sum_{e=1}^{N_e} \sum_{i=1}^{N_A^e} \varepsilon_i^e = \sum_{e=1}^{N_e} \sum_{i=1}^{N_A^e} \sum_{t=1}^{N_T^e} \tilde{w}_t^e k(\mathbf{x}_i^e, \tilde{\mathbf{x}}_t^e) \quad (2)$$

where ε_i^e are the atomic energies, e is the index that runs over the distinct chemical elements, i is the index that runs over the different atoms for each element type, N_e is the total number of elements, and N_A^e is the total number of atoms of the element indexed by e . In addition, \tilde{w}_t^e are the weights, and $k(\mathbf{x}_i^e, \tilde{\mathbf{x}}_t^e)$ is a kernel that measures the distance between the descriptor vectors \mathbf{x}_i^e and $\tilde{\mathbf{x}}_t^e$, the latter belonging to the training dataset for the chemical element indexed by e , which has N_T^e such descriptors. We choose the polynomial kernel⁵⁸:

$$k(\mathbf{x}_i^e, \tilde{\mathbf{x}}_t^e) = \left(\frac{\mathbf{x}_i^e \cdot \tilde{\mathbf{x}}_t^e}{|\mathbf{x}_i^e| |\tilde{\mathbf{x}}_t^e|} \right)^{\xi}, \quad (3)$$

where the exponent ξ is a parameter used to control the sharpness of the kernel. In addition, we employ the Smooth Overlap of Atomic Positions (SOAP) formalism⁵⁸, where the rotationally invariant descriptors correspond to the power spectrum of the coefficients c_i^e :

$$[\mathbf{x}_i^e]_{n_1 n_2 l}^{e_1 e_2} = \sqrt{\frac{8\pi^2}{2l+1}} \sum_{m=-l}^l c_{i,e_1,n_1 l m}^e c_{i,e_2,n_2 l m}^{e*}, \quad (4)$$

where $e_1, e_2 \in \{1, 2, \dots, N_e\}$, $n_1, n_2 \in \{1, 2, \dots, N_r\}$, and $l \in \{0, 1, \dots, L_{\text{max}}\}$ are used to index the components of the descriptor, a vector of length $N_r^2 N_e^2 (L_{\text{max}} + 1)$. The coefficients c_i^e themselves arise during the basis expansion of the atom density for the atom positioned at $\mathbf{r}_i^e := (r_{i_1}^e, r_{i_2}^e, r_{i_3}^e)$:

$$b_{i,\bar{e}}^e(\mathbf{r} - \mathbf{r}_i^e) = \sum_{l=0}^{L_{\text{max}}} \sum_{m=-l}^l \sum_{n=1}^{N_r} c_{i,\bar{e},nlm}^e j_l(q_{nl} |\mathbf{r} - \mathbf{r}_i^e|) Y_{lm}(\mathbf{r} - \mathbf{r}_i^e), \quad (5)$$

where $\bar{e} \in \{1, \dots, N_e\}$, N_r is the number of radial basis functions for each l , L_{max} is the maximum value of l , Y_{lm} are the spherical harmonics, and j_l are the normalized spherical Bessel functions, with q_{nl} chosen such that $j_l(q_{nl} R_{\text{cut}}) = 0$, R_{cut} being the region of influence for any atom, i.e., the distance within which the atoms are assumed to contribute to the atom density. Since the chosen basis is complete, it allows for systematic convergence. The atom density itself is calculated as⁵⁷:

$$b_{i,\bar{e}}^e(\mathbf{r} - \mathbf{r}_i^e) = \sum_{j=1}^{N_A^{\bar{e}}} f_{\text{cut}}(|\mathbf{r}_{\bar{e}}^j - \mathbf{r}_i^e|) g(\mathbf{r} - \mathbf{r}_{\bar{e}}^j + \mathbf{r}_i^e), \quad (6)$$

where f_{cut} is the cosine function⁵⁹, and g is the Gaussian function:

$$g(\mathbf{r} - \mathbf{r}_{\bar{e}}^j + \mathbf{r}_i^e) = \frac{1}{\sqrt{2\sigma_a^2\pi}} \exp\left(-\frac{|\mathbf{r} - \mathbf{r}_{\bar{e}}^j + \mathbf{r}_i^e|^2}{2\sigma_a^2}\right), \quad (7)$$

with σ_a being the standard deviation of the Gaussian. A smaller value of σ_a is suitable for systems with significant heterogeneity, while a larger value of σ_a is suitable for systems that are homogeneous. On using the single center expansion of the Gaussian function⁶⁰, the coefficients c_i^e can be written as^{58,61}:

$$c_{i,\bar{e},nlm}^e = \sum_{j=1}^{N_A^{\bar{e}}} h_{nl}(|\mathbf{r}_{\bar{e}}^j - \mathbf{r}_i^e|) Y_{lm}^*(\mathbf{r}_{\bar{e}}^j - \mathbf{r}_i^e), \quad (8)$$

where the function h_{nl} itself takes the form:

$$h_{nl}(r) = C(r) \int_0^{R_{\text{cut}}} j_l(q_{nl} r') \exp\left(-\frac{r'^2 + r^2}{2\sigma_a^2}\right) l_l\left(\frac{rr'}{\sigma_a^2}\right) r'^2 dr', \quad (9)$$

with $C(r) = 4\pi f_{\text{cut}}(r) / \sqrt{2\sigma_a^2\pi}$, and l_l being the modified spherical Bessel function of the first kind.

The above described model for E_{Δ} also provides access to derivatives with respect to atomic positions. In particular, the first-order derivative of E_{Δ} with respect to atomic position provides a correction to the force computed by orbital-free DFT:

$$\begin{aligned} f_{\Delta,j\alpha}^{\bar{e}} &= -\frac{\partial E_{\Delta}}{\partial r_{j\alpha}^{\bar{e}}} \\ &= -\sum_{e=1}^{N_e} \sum_{i=1}^{N_A^e} \sum_{t=1}^{N_T^e} \tilde{w}_t^e \frac{\partial k(\mathbf{x}_i^e, \tilde{\mathbf{x}}_t^e)}{\partial \mathbf{x}_i^e} \cdot \frac{\partial \mathbf{x}_i^e}{\partial r_{j\alpha}^{\bar{e}}} \\ &= \sum_{e=1}^{N_e} \sum_{i=1}^{N_A^e} \sum_{t=1}^{N_T^e} \tilde{w}_t^e \xi k(\mathbf{x}_i^e, \tilde{\mathbf{x}}_t^e) \mathbf{z}_{i,t} \cdot \frac{\partial \mathbf{x}_i^e}{\partial r_{j\alpha}^{\bar{e}}}, \end{aligned} \quad (10)$$

where

$$\mathbf{z}_{i,l}^e = \left(\frac{\mathbf{x}_i^e}{\mathbf{x}_i^e \cdot \mathbf{x}_i^e} - \frac{\tilde{\mathbf{x}}_i^e}{\mathbf{x}_i^e \cdot \tilde{\mathbf{x}}_i^e} \right), \quad (11a)$$

$$\frac{\partial [\mathbf{x}_i^e]_{n_1 n_2 l}^{e_1 e_2}}{\partial r_{j\alpha}^e} = c_l \sum_{m=-l}^l \left(\frac{\partial c_{i,e_1,n_1lm}^e}{\partial r_{j\alpha}^e} c_{i,e_2,n_2lm}^{e*} + c_{i,e_1,n_1lm}^e \frac{\partial c_{i,e_2,n_2lm}^{e*}}{\partial r_{j\alpha}^e} \right). \quad (11b)$$

Above, $c_l = \sqrt{8\pi^2/(2l+1)}$, and the derivatives of c_i^e can be obtained to be:

$$\frac{\partial c_{i,\tilde{e},nlm}^e}{\partial r_{j\alpha}^e} = \begin{cases} \left(\frac{r_{j\alpha}^e - r_{i\alpha}^e}{|\mathbf{r}_j^e - \mathbf{r}_i^e|} h'_{nl} \left(|\mathbf{r}_j^e - \mathbf{r}_i^e| \right) Y_{lm}^* \left(\mathbf{r}_j^e - \mathbf{r}_i^e \right) \right. \\ \left. + h_{nl} \left(|\mathbf{r}_j^e - \mathbf{r}_i^e| \right) \frac{\partial Y_{lm}^* \left(\mathbf{r}_j^e - \mathbf{r}_i^e \right)}{\partial (r_{j\alpha}^e - r_{i\alpha}^e)} \right), & \text{if } j \neq i, \\ -\sum_{k=1, k \neq i}^{N_A^e} \frac{\partial c_{i,\tilde{e},nlm}^e}{\partial r_{k\alpha}^e}, & \text{if } j = i, \end{cases} \quad (12)$$

where h'_{nl} denotes the derivative of h_{nl} . Similarly, the correction to the stress tensor, which represents the first-order derivative of E_Δ with respect to the strain tensor/deformation gradient, has been presented in Appendix A.

B. Training: Bayesian linear regression

The expressions for the energy and atomic forces appearing in Eqs. 2 and 10, respectively, can be written in matrix form as:

$$E_\Delta^s = \sum_{e=1}^{N_e} \mathbf{K}_E^{s,e} \mathbf{w}^e, \quad \mathbf{f}_\Delta^s = \sum_{e=1}^{N_e} \mathbf{K}_f^{s,e} \mathbf{w}^e, \quad s \in \{1, \dots, N_{st}\}, \quad (13)$$

where s is an index introduced for denoting the configuration/structure, $\mathbf{w}^e \in \mathbb{R}^{N_T^e \times 1}$ is a vector of the weights, $\mathbf{K}_E^{s,e} \in \mathbb{R}^{1 \times N_T^e}$ is the covariance matrix for the energy, and $\mathbf{K}_f^{s,e} \in \mathbb{R}^{(3 \sum_e N_A^e) \times N_T^e}$ is the covariance matrix for the forces. For numerical purposes, the energy and forces are dimensionless:

$$E_\Delta^s := \frac{E_\Delta - \mu_E}{\sigma_E}, \quad \mathbf{f}_\Delta^s := \frac{\mathbf{f}_\Delta}{\sigma_f}, \quad (14)$$

where μ_E and σ_E are the mean and standard deviation of E_Δ^s , respectively, and σ_f is the standard deviation of \mathbf{f}_Δ^s , all defined over the different structures.

The model weights \mathbf{w}^e need to be determined from the data available for training. To do so, we consider Bayesian linear regression, which involves minimizing the loss function⁶²:

$$\mathcal{L}(\mathbf{w}) = \frac{\beta}{2} \left(w_E^2 \left\| \mathbf{y}_E - \sum_{e=1}^{N_e} \mathbf{K}_E^e \mathbf{w}^e \right\|_2^2 + w_f^2 \left\| \mathbf{y}_f - \frac{\sigma_E}{\sigma_f} \sum_{e=1}^{N_e} \mathbf{K}_f^e \mathbf{w}^e \right\|_2^2 \right) - \frac{\alpha}{2} \|\mathbf{w}\|_2^2, \quad (15)$$

where

$$\mathbf{w} = [\mathbf{w}^1; \mathbf{w}^2; \dots; \mathbf{w}^{N_e}] \quad (16a)$$

$$\mathbf{K}_E^e = [\mathbf{K}_E^{1,e}; \mathbf{K}_E^{2,e}; \dots; \mathbf{K}_E^{N_{st},e}], \quad (16b)$$

$$\mathbf{K}_f^e = [\mathbf{K}_f^{1,e}; \mathbf{K}_f^{2,e}; \dots; \mathbf{K}_f^{N_{st},e}], \quad (16c)$$

$$\mathbf{y}_E = [E_\Delta^1; E_\Delta^2; \dots; E_\Delta^{N_{st}}], \quad (16d)$$

$$\mathbf{y}_f = [\mathbf{f}_\Delta^1; \mathbf{f}_\Delta^2; \dots; \mathbf{f}_\Delta^{N_{st}}], \quad (16e)$$

with the semicolon used as a delimiter between the different rows of the vector/matrix. Above, α and β are parameters, while w_E and w_f are the weighting factors for the errors in the energy and forces, respectively. The optimized weights can then be written as:

$$\mathbf{w} = \beta \mathbf{C}_w (\mathbf{K}_E^T \mathbf{y}_E + \mathbf{K}_f^T \mathbf{y}_f), \quad (17)$$

where

$$\mathbf{C}_w = (\alpha I + \beta (\mathbf{K}_E^T \mathbf{K}_E + \mathbf{K}_f^T \mathbf{K}_f))^{-1}, \quad (18)$$

with the matrices $\mathbf{K}_E \in \mathbb{R}^{N_{st} \times (\sum_e N_T^e)}$ and $\mathbf{K}_f \in \mathbb{R}^{N_{st} \times (3 \sum_e N_A^e) \times (\sum_e N_T^e)}$ of the form:

$$\mathbf{K}_E = [\mathbf{w}_E \mathbf{K}_E^1; \mathbf{w}_E \mathbf{K}_E^2; \dots; \mathbf{w}_E \mathbf{K}_E^{N_e}], \quad (19a)$$

$$\mathbf{K}_f = \left[w_f \frac{\sigma_E}{\sigma_f} \mathbf{K}_f^1; w_f \frac{\sigma_E}{\sigma_f} \mathbf{K}_f^2; \dots; w_f \frac{\sigma_E}{\sigma_f} \mathbf{K}_f^{N_e} \right]. \quad (19b)$$

These optimized weights can then be used in Eq. 13 to predict the energy and forces for any new structure, after having calculated the structure's covariance matrices for the energy and forces. The uncertainty in the energy (σ_{y_E}) and forces (σ_{y_f}) so calculated can be estimated as:

$$\sigma_{y_E}^2 = \text{diag} \left(\frac{1}{\beta} + \mathbf{K}_E \mathbf{C}_w \mathbf{K}_E^T \right), \quad (20a)$$

$$\sigma_{y_f}^2 = \text{diag} \left(\frac{1}{\beta} + \mathbf{K}_f \mathbf{C}_w \mathbf{K}_f^T \right), \quad (20b)$$

where $\text{diag}(\cdot)$ refers to the diagonal of the matrix.

III. RESULTS AND DISCUSSION

We have implemented the above described Δ -machine learning formalism, henceforth referred to as Δ_{OF} -MLFF, within the SPARC electronic structure code^{63–66}. In particular, we have developed a framework for on-the-fly MD simulations, as outlined in Fig. 1. In such simulations, after a few initial training MD steps for which Kohn-Sham calculations are performed, the energy and atomic forces are set to those predicted by the Δ_{OF} -MLFF model, except when the uncertainty in the forces so computed is larger than a specified threshold σ_{tol} , at which point the energy and forces are set to those from a Kohn-Sham calculation, which are then also included into the training dataset. Though the current work is focused on energy and atomic forces, the implementation has the capability to also include the stress tensor as part of the training

and prediction. The threshold σ_{tol} is made to be adaptive by setting it to the maximum value of σ_{y_f} obtained in the $\Delta_{\text{OF}}\text{-MLFF}$ step that is subsequent to a training step⁶¹. Though this strategy results in increased number of Kohn-Sham calculations in the beginning of the MD simulation, the frequency of such calculations decreases rapidly, whereby the total number of Kohn-Sham calculations in the total MD simulation is generally lower than for other less stringent σ_{tol} choices. To avoid the cubic scaling bottleneck encountered in training, a two-step data selection procedure is employed: for any given configuration, we only add those atoms to the training dataset for which the Bayesian error in forces exceeds σ_{tol} , and then perform CUR⁶¹ on the resulting dataset for downsampling^{61,67,68}. Note that the parameters α and β are also dynamically updated within each training step, by maximizing the evidence function of Bayesian linear regression⁶².

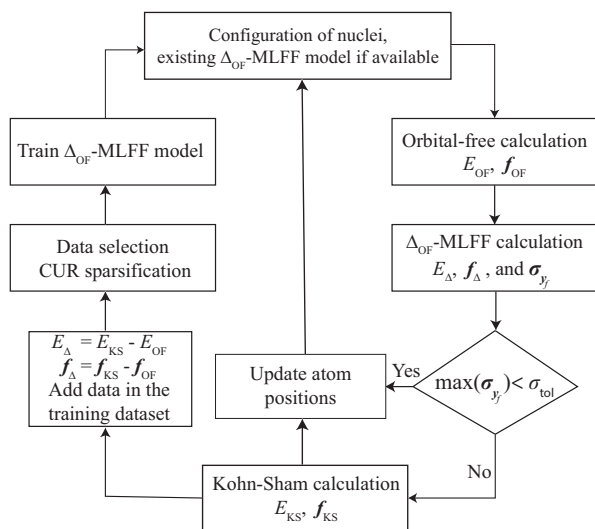


FIG. 1. Outline of on-the-fly MD simulations using $\Delta_{\text{OF}}\text{-MLFF}$.

To study the sensitivity to parameters, accuracy, and efficiency of the $\Delta_{\text{OF}}\text{-MLFF}$ scheme, we consider the following systems: aluminum (Al) at 300 K, silicon (Si) at 300 K, and molten alloy of aluminum-silicon ($\text{Al}_{0.88}\text{Si}_{0.12}$) at 1473 K. We consider 108-, 216-, and 500-atom cells of Al, Si, and $\text{Al}_{0.88}\text{Si}_{0.12}$, respectively. As an application, we also study Si aggregation in $\text{Al}_{0.88}\text{Si}_{0.12}$. In all instances, we perform isokinetic ensemble (NVK) MD with Gaussian thermostat⁶⁹ and time steps of 4, 4, and 2 fs for the Al, Si, and $\text{Al}_{0.88}\text{Si}_{0.12}$ systems, respectively. In the Kohn-Sham calculations, we employ optimized norm-conserving Vanderbilt (ONCV) pseudopotentials⁷⁰ from the SPMS set⁷¹, and the following exchange-correlation functionals: local density approximation (LDA)⁷² for Al, and the Perdew-Burke-Ernzerhof (PBE)⁷³ variant of the generalized gradient approximation (GGA) for Si and $\text{Al}_{0.88}\text{Si}_{0.12}$. In the orbital-free calculations, which are also performed using a real-space formalism^{74,75}, we employ the Thomas-Fermi-von Weizsäcker (TFW) kinetic energy functional⁷⁶ (weight factor $\lambda = 1$), LDA exchange-correlation functional, and bulk-derived local pseudopotentials (BLPS)⁷⁷. Note that we have

chosen a rather simple kinetic energy functional, since it suffices for achieving the target accuracy for the MD simulations in this work. Indeed, choosing more sophisticated kinetic energy functionals^{11–17,20–31,78} is likely to further increase the accuracy of the $\Delta_{\text{OF}}\text{-MLFF}$ scheme, but will also substantially increase the cost.

In presentation of the results, we compare against orbital-free DFT (OF-DFT) as well as MLFF learnt directly from Kohn-Sham DFT (KS-MLFF), i.e., same scheme used for machine learning E_{KS} and the corresponding atomic forces instead. Indeed, OF-DFT and KS-MLFF can be considered to be the limiting cases of the $\Delta_{\text{OF}}\text{-MLFF}$ scheme. All errors are defined with respect to results obtained from Kohn-Sham DFT (KS-DFT). The energy error is defined to be the magnitude of the difference, and the force error is defined to be the maximum difference (in magnitude) in any force component among all the atoms. The errors are averaged over a sufficient number of MD steps to put statistical errors well below the errors under consideration.

A. Sensitivity to parameters

We now study the sensitivity of $\Delta_{\text{OF}}\text{-MLFF}$ to the key parameters inherent to the model: hyperparameters in the machine learning model, and the discretization parameters in the orbital-free and Kohn-Sham calculations that are performed. The focus here is on the atomic force errors, since the qualitative trends for the energy errors are similar, with the values generally being one order of magnitude smaller.

First, we study the variation in the $\Delta_{\text{OF}}\text{-MLFF}$ errors with respect to the hyperparameters N_r , L_{max} , R_{max} , and σ_a , the results so obtained are presented and compared with KS-MLFF in Fig. 2. The Kohn-Sham calculations employ Γ -point for Brillouin zone integration. Both orbital-free and Kohn-Sham calculations employ mesh sizes of 0.35, 0.35, and 0.32 bohr for the Al, Si, and $\text{Al}_{0.88}\text{Si}_{0.12}$ systems, respectively, which translates to the energy and forces being converged to within 10^{-4} ha/bohr and 10^{-5} ha/atom, respectively. We observe that $\Delta_{\text{OF}}\text{-MLFF}$ has consistently smaller errors relative to KS-MLFF. Furthermore, the errors in $\Delta_{\text{OF}}\text{-MLFF}$ have significantly smaller variation with respect to σ_a , and saturate more rapidly with respect to the other hyperparameters, leading to more efficient MLFF training/prediction as well as improved robustness and efficiency with respect to hyperparameter optimization. For the remainder of this work, we select the following hyperparameter values for $\Delta_{\text{OF}}\text{-MLFF}$: $\{R_{\text{cut}}, N_r, L_{\text{max}}, \sigma_a\} = \{8, 8, 3, 1\}$, $\{8, 6, 4, 1\}$, and $\{8, 6, 4, 1\}$ for the Al, Si, and $\text{Al}_{0.88}\text{Si}_{0.12}$ systems, respectively. The corresponding values for KS-MLFF are $\{10, 8, 6, 1\}$, $\{10, 8, 5, 1\}$, and $\{10, 8, 5, 1\}$, respectively. The values have been chosen such that larger values of R_{cut} , N_r , and L_{max} , or different values of σ_a , do not provide any noticeable increase in the accuracy.

Next, we study the variation in the $\Delta_{\text{OF}}\text{-MLFF}$ force errors with mesh size, the results so obtained are presented and compared with OF-DFT and KS-MLFF in Fig. 3. The Kohn-Sham calculations again employ Γ -point for Brillouin zone integration. We observe that the Δ -MLFF errors are not only signifi-

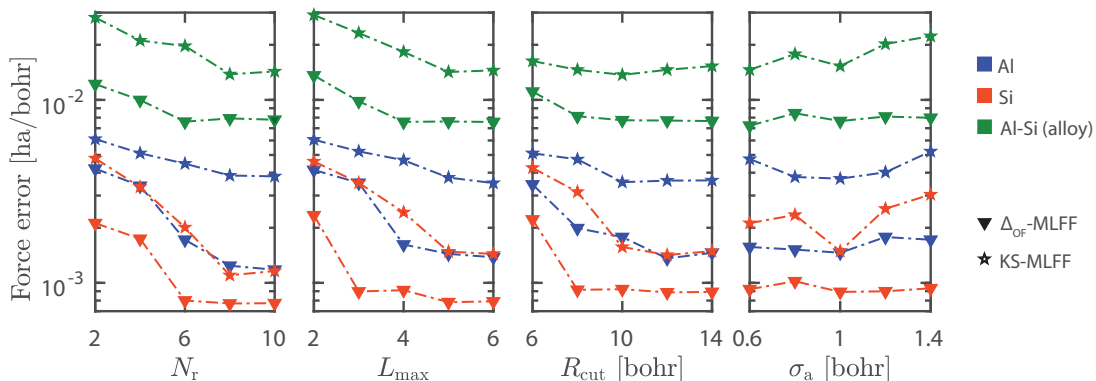


FIG. 2. Variation in the force error with respect to the model hyperparameters for the Al, Si, and $\text{Al}_{0.88}\text{Si}_{0.12}$ systems, averaged over 2000 MD steps.

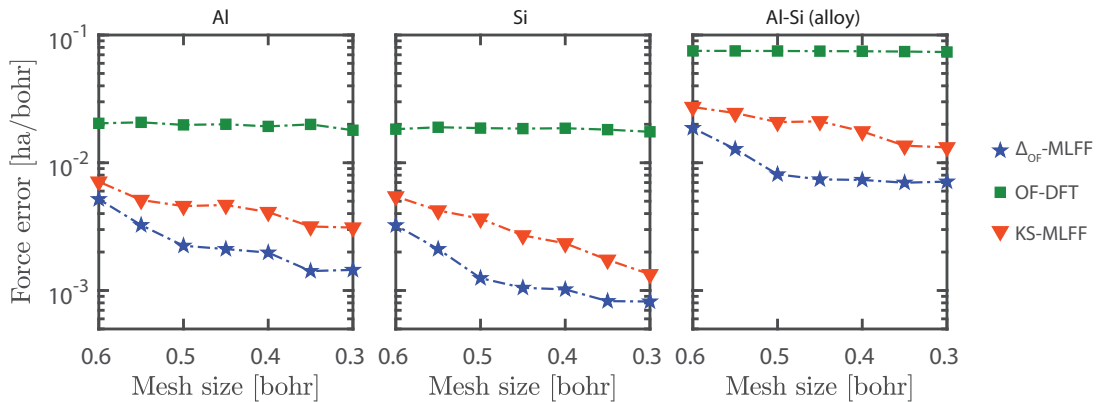


FIG. 3. Variation in the force error with mesh size for the Al, Si, and $\text{Al}_{0.88}\text{Si}_{0.12}$ systems, averaged over 1000 MD steps.

cantly smaller than KS-MLFF errors for any given mesh size, but are also less sensitive, suggesting that a coarser grid can be used for $\Delta_{\text{OF-MLFF}}$ relative to KS-MLFF. In addition, the OF-DFT errors are insensitive to the mesh size, suggesting that the error is completely dominated by the physical error in OF-DFT. The physical error in $\Delta_{\text{OF-MLFF}}$ appears to be smaller than KS-MLFF, both being significantly lower than OF-DFT, as confirmed below.

Finally, we study the variation in the $\Delta_{\text{OF-MLFF}}$ force errors with number of Monkhorst-Pack wavevectors at which Brillouin zone integration is performed in KS-DFT, i.e., k-points. The results so obtained are presented and compared with OF-DFT and KS-MLFF in Fig. 4. As before, both orbital-free and Kohn-Sham calculations employ mesh sizes of 0.35, 0.35, and 0.32 bohr for the Al, Si, and $\text{Al}_{0.88}\text{Si}_{0.12}$ systems, respectively, which translates to the energy and forces being converged to within 10^{-4} ha/bohr and 10^{-5} ha/atom, respectively. We observe that the Δ -MLFF errors are not only significantly smaller than KS-MLFF errors for any given number of k-points, but are also less sensitive, suggesting that a coarser k-point grid can be used in $\Delta_{\text{OF-MLFF}}$ relative to KS-MLFF. In addition, the OF-DFT errors are insensitive to the number of k-points used in KS-DFT, confirming that the error is completely dominated by the physical error in OF-DFT. The physical error in $\Delta_{\text{OF-MLFF}}$ is confirmed to

be smaller than KS-MLFF, both being significantly lower than OF-DFT.

B. Accuracy

We now study the accuracy of the $\Delta_{\text{OF-MLFF}}$ scheme. To do so, we choose orbital-free and Kohn-Sham parameters, including the mesh size and number of k-points, to be such that the energy and atomic forces are converged to within 10^{-5} ha/atom and 10^{-4} ha/bohr, respectively. This translates to mesh sizes of 0.35, 0.35, and 0.32 bohr for the Al, Si, and $\text{Al}_{0.88}\text{Si}_{0.12}$ systems, respectively. The corresponding k-point grids are $5 \times 5 \times 5$, $2 \times 2 \times 2$, and $3 \times 3 \times 3$, respectively. We present the results so obtained in Table I and compare it with those obtained by OF-DFT as well as KS-MLFF. We observe that $\Delta_{\text{OF-MLFF}}$ reduces the OF-DFT energy and force errors by more than two orders of magnitude, bringing it close to the accuracy typically desired in KS-DFT MD simulations. In so doing, it is also more accurate than KS-MLFF, by $\sim 50\%$, 50% , and 20% in the energy, and by 35% , 35% , and 30% in the forces, for the Al, Si, and $\text{Al}_{0.88}\text{Si}_{0.12}$ systems, respectively. Note that the accuracy of both $\Delta_{\text{OF-MLFF}}$ and KS-MLFF is significantly lower for liquid $\text{Al}_{0.88}\text{Si}_{0.12}$ compared to solid Al and Si. This can be attributed to the larger

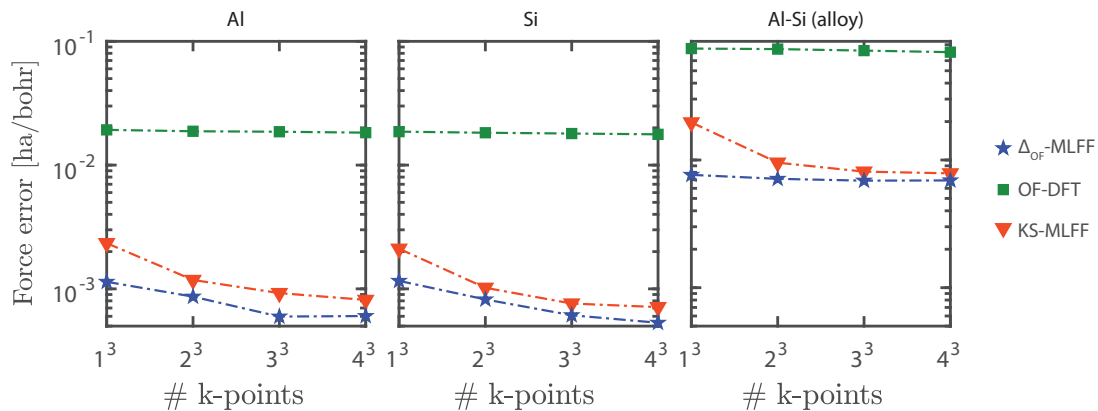


FIG. 4. Variation in the force error with number of k-points for the Al, Si, and $\text{Al}_{0.88}\text{Si}_{0.12}$ systems, averaged over 1000 MD steps.

configurational space and higher forces in the liquid system. Indeed, the relative accuracy in energy and atomic forces is comparable for all three systems.

The orders of magnitude improvement of $\Delta_{\text{OF}}\text{-MLFF}$ over OF-DFT is not surprising, given the rather primitive local/semilocal nature of the TFW kinetic energy functional. In particular, even though the electron density from TFW OF-DFT is found to be *close* to KS-DFT, the energies and consequently the forces are found to be substantially different⁵⁶. The use of more sophisticated kinetic energy functionals^{10,16–19} is likely to increase the accuracy of not only OF-DFT, but also $\Delta_{\text{OF}}\text{-MLFF}$. The ability of the $\Delta_{\text{OF}}\text{-MLFF}$ scheme to achieve higher accuracy than KS-MLFF can be attributed in part to the smoother and more localized nature of E_{Δ} relative to E_{KS} , which makes it more amenable to machine learning. Indeed, the use of more advanced kinetic energy functionals in the orbital-free calculations is likely to widen the gap. Notably, the cancellation of long range electrostatic effects in E_{Δ} is likely to make $\Delta_{\text{OF}}\text{-MLFF}$ significantly more accurate than KS-MLFF for polar systems. Such systems have not been considered here due to the paucity of accurate and transferable pseudopotentials in OF-DFT.

C. Performance

We now study the performance of the $\Delta_{\text{OF}}\text{-MLFF}$ scheme. To do so, we choose all parameters, including mesh size, k-points, and hyperparameters, to be such that the atomic forces in the $\Delta_{\text{OF}}\text{-MLFF}$ scheme are accurate to within 2×10^{-3} , 2×10^{-3} , and 10^{-2} ha/bohr for the Al, Si, and $\text{Al}_{0.88}\text{Si}_{0.12}$ systems, respectively. To facilitate comparison, the mesh sizes and number of k-points in KS-MLFF are also chosen to be such that they provide the aforementioned accuracy in the forces, i.e., same accuracy as $\Delta_{\text{OF}}\text{-MLFF}$. Note that we do not compare against OF-DFT here since it is not able to achieve this desired accuracy. In fact, the errors in OF-DFT are more than an order of magnitude larger than the accuracy targeted here, as shown in the previous subsection.

We present the results so obtained in Table II, which also contains the mesh sizes and number of k-points chosen for

each scheme. We observe that both $\Delta_{\text{OF}}\text{-MLFF}$ and KS-MLFF perform Kohn-Sham calculations on only $\sim 1\%$ of the steps in the MD simulation containing a total of 10,000 steps, with the number of such calculations in $\Delta_{\text{OF}}\text{-MLFF}$ being lower than KS-MLFF by $\sim 25\%$, 25% , and 15% for the Al, Si, and $\text{Al}_{0.88}\text{Si}_{0.12}$ systems, respectively. Indeed, most of the the Kohn-Sham calculations are performed in the beginning of the MD simulation, with lowering frequency as the simulation progresses, as can be seen in Fig. 5. We also observe that even though the $\Delta_{\text{OF}}\text{-MLFF}$ scheme requires an orbital-free calculation to be performed in each MD step, the overall time is still significantly lower than KS-MLFF, being $\sim 1.5\times$, $\sim 1.05\times$, and $\sim 3.15\times$ faster for the Al, Si, and $\text{Al}_{0.88}\text{Si}_{0.12}$ systems, respectively. This is because the computational expense is primarily determined by the cost of the Kohn-Sham calculations, for which the ability to use coarser real space and k-point grids in $\Delta_{\text{OF}}\text{-MLFF}$, as well as the need to perform fewer such calculations relative to KS-MLFF, can provide substantial savings. This becomes especially true as the system size increases, due to the cubic scaling nature of Kohn-Sham calculations relative to the linear scaling nature of orbital-free and MLFF calculations. Note that there is significant scope of improvement in the current OF-DFT implementation, including the use of preconditioners, which is likely to further increase the efficiency of the $\Delta_{\text{OF}}\text{-MLFF}$ scheme. Also note that though the predicted error and the true error can differ by around an order of magnitude (Fig. 5), they are well-correlated, the correlation coefficient being 0.65 – 0.70, which is similar to that obtained for the KS-MLFF scheme, both here and in literature⁶¹. Indeed, this difference between the true and predicted error is system dependent and is therefore not known a priori.

D. Application: structure of molten $\text{Al}_{0.88}\text{Si}_{0.12}$

We now apply the $\Delta_{\text{OF}}\text{-MLFF}$ scheme to study the possibility of Si aggregation in the molten $\text{Al}_{0.88}\text{Si}_{0.12}$ alloy. Experiments have measured a spatial variation in the density of molten $\text{Al}_{0.88}\text{Si}_{0.12}$, which has been attributed to Si aggregation and the formation of Si clusters within the alloy⁷⁹. This was however contradicted by KS-DFT simulations⁸⁰, though

Material system	Energy error [ha/atom] ($\times 10^{-5}$)			Force error [ha/bohr] ($\times 10^{-4}$)		
	$\Delta_{\text{OF-MLFF}}$	OF-DFT	KS-MLFF	$\Delta_{\text{OF-MLFF}}$	OF-DFT	KS-MLFF
Al	3.1	776.2	6.2	5.1	170.2	7.9
Si	2.8	726.7	5.9	4.2	192.1	6.3
$\text{Al}_{0.88}\text{Si}_{0.12}$	6.9	2651.3	8.5	61.3	735.9	88.2

TABLE I. Energy and force errors in $\Delta_{\text{OF-MLFF}}$, OF-DFT, and KS-MLFF, averaged over 1000 MD steps.

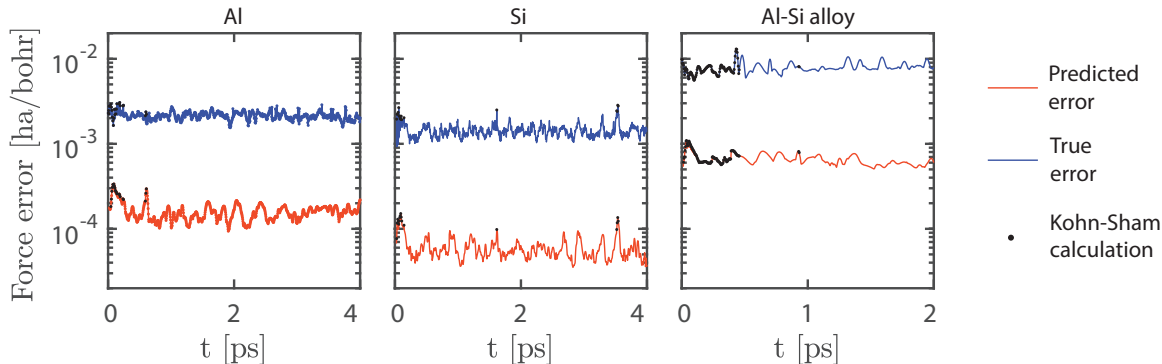


FIG. 5. Variation of the true and predicted force error in $\Delta_{\text{OF-MLFF}}$ for a MD simulation of 1000 steps. The steps where Kohn-Sham calculations have been performed are also indicated.

the relatively small length (500-atom cell) and time scales (10 ps) associated with these simulations has been suggested as a possible reason for the disagreement, which provides the motivation for the current study.

First, we verify the scheme’s accuracy for this application by calculating the pair distribution functions (PDFs) for the alloy, and comparing it with those obtained by OF-DFT and KS-DFT. As before, we consider a 500-atom cell at a temperature of 1473 K, Γ -point Brillouin zone integration in Kohn-Sham calculations, 12-th order finite-differences with mesh size of 0.55 bohr, which provides an accuracy of 10^{-4} ha/atom and 10^{-2} ha/bohr in the energy and atomic forces, respectively, in both orbital-free and Kohn-Sham calculations, and NVK MD simulations with Gaussian thermostat and a timestep of 2 fs, for a total of 10,000 steps. Note that PDFs are well-converged with respect to all the parameters in the orbital-free and Kohn-Sham calculations, the results so obtained presented in Fig. 6. We observe that the PDFs from $\Delta_{\text{OF-MLFF}}$ are nearly indistinguishable to those from KS-DFT, while those from OF-DFT are significantly different, which demonstrates the substantially increased accuracy of the $\Delta_{\text{OF-MLFF}}$ scheme relative to OF-DFT. Note that the PDFs obtained here are also in good agreement with those in literature obtained using KS-DFT⁸⁰, further verifying the accuracy of the simulations.

Next, we perform the MD simulation with a 5000-atom cell for 50,000 steps, i.e., a total time of 100 ps. All parameters are identical to those used for the calculation of the PDFs. The Δ -MLFF model trained during the 500-atom MD simulation is used as the initial model for the 5000-atom simulation, a strategy referred to as transfer learning. In so doing, the complete simulation requires only six Kohn-Sham calculations, thereby providing significant computational savings. To examine the aggregation of Si atoms, we analyze the distribution of the Al and Si neighbors, as depicted in Fig. 7. We observe that the

ratio of Al to Si nearest neighbors aligns closely with that expected from a random distribution, indicating a homogeneous chemical mixing in the system. In addition, the most common coordination for the Si atoms is nine Al atoms and zero Si atoms in the nearest neighbor shell. Notably, there are very few Si atoms with more than two Si nearest neighbors and virtually none with more than four. Though these results correspond to 1473 K, we have verified that the qualitative features remain unchanged at 1000 and 1200 K. Indeed, the results are nearly identical to those for the 500-atom cell, which are also in very good agreement with the aforementioned KS-DFT investigation⁸⁰. Therefore, the current results do not support the hypothesis of silicon aggregation⁷⁹, in agreement with previous KS-DFT⁸⁰ and force field simulations⁸¹.

IV. CONCLUDING REMARKS

In this work, we have presented a Δ -machine learning model for obtaining Kohn-Sham accuracy from orbital-free DFT calculations. In particular, a MLFF scheme based on the kernel method, with SOAP descriptors and weights determined through Bayesian linear regression, has been employed for capturing the differences between the Kohn-Sham and orbital-free DFT energies/forces, the resulting formalism referred to as $\Delta_{\text{OF-MLFF}}$. We have implemented $\Delta_{\text{OF-MLFF}}$ in the context of on-the-fly MD simulations, whose accuracy, performance, and sensitivity to parameters has been studied for the aluminum, silicon, and molten aluminum silicon alloy ($\text{Al}_{0.88}\text{Si}_{0.12}$) systems. We have found that $\Delta_{\text{OF-MLFF}}$ is not only more accurate than TFW orbital-free DFT by more than two orders of magnitude, but is also more accurate than MLFFs generated solely from Kohn-Sham DFT, while being more efficient and less sensitive to the model parameters. We

Material system	Method	Discretization parameters		# Kohn-Sham steps performed	Time [CPU hours]			
		Mesh size [bohr]	k-point grid		Kohn-Sham	MLFF	Orbital-free	Total
Al	$\Delta_{\text{OF}}\text{-MLFF}$	0.55	$1 \times 1 \times 1$	66	2.9	18.1	34.2	55.2
	KS-MLFF	0.35	$2 \times 2 \times 2$	87	63.2	18.4	-	81.6
Si	$\Delta_{\text{OF}}\text{-MLFF}$	0.55	$1 \times 1 \times 1$	55	5.5	32.1	62.2	99.8
	KS-MLFF	0.35	$1 \times 1 \times 1$	76	61.4	42.7	-	104.1
$\text{Al}_{0.88}\text{Si}_{0.12}$	$\Delta_{\text{OF}}\text{-MLFF}$	0.55	$1 \times 1 \times 1$	89	45.3	152.1	196.1	393.5
	KS-MLFF	0.35	$2 \times 2 \times 2$	103	1079.2	156.1	-	1235.3

TABLE II. Computational time of $\Delta_{\text{OF}}\text{-MLFF}$ and KS-MLFF for a MD simulation of 10,000 steps.

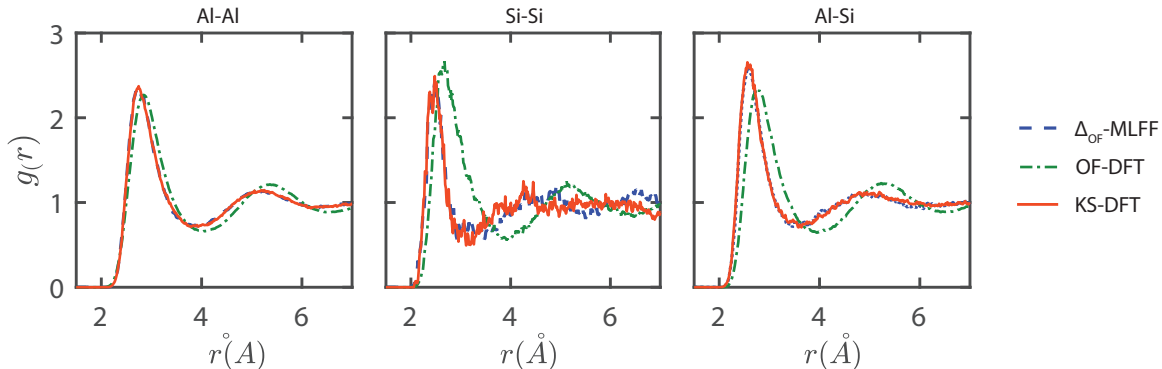


FIG. 6. Pair distribution functions for the molten $\text{Al}_{0.88}\text{Si}_{0.12}$ alloy at 1473 K, as computed by $\Delta_{\text{OF}}\text{-MLFF}$, OF-DFT, and KS-DFT.

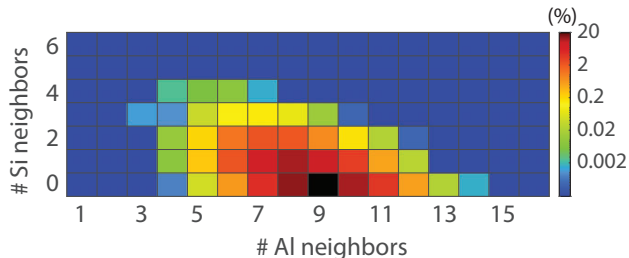


FIG. 7. Distribution of Al and Si neighbors for Si atoms in molten $\text{Al}_{0.88}\text{Si}_{0.12}$ at 1473 K, as computed using $\Delta_{\text{OF}}\text{-MLFF}$.

have applied the $\Delta_{\text{OF}}\text{-MLFF}$ scheme to study the structure of molten $\text{Al}_{0.88}\text{Si}_{0.12}$, for which we have found no evidence of Si aggregation, in agreement with a previous Kohn-Sham DFT investigation performed at an order of magnitude smaller length and time scales.

The use of more advanced kinetic energy functionals for the orbital-free calculations in the $\Delta_{\text{OF}}\text{-MLFF}$ scheme is likely to further increase its accuracy. In this context, the choice/development of functionals that have the best balance between accuracy and computational cost is a worthy subject for future research. The implementation of $\Delta_{\text{OF}}\text{-MLFF}$ on GPUs is likely to significantly bring down the solution times, as demonstrated recently for the associated Kohn-Sham calculations⁸², making it another subject worthy for future research. From a MLFF perspective, the current findings suggest that orbital-free DFT and other fast physical approximations can provide a valuable complement to machine learning techniques, indicating that renewed focus on improving the

speed, accuracy, and general applicability of orbital-free DFT is warranted.

ACKNOWLEDGMENTS

The authors gratefully acknowledge the support of the U.S. Department of Energy, Office of Science under grant DE-SC0023445. This work was performed, in part, under the auspices of the U.S. Department of Energy by Lawrence Livermore National Laboratory under Contract DE-AC52-07NA27344. This research was also supported by the supercomputing infrastructure provided by Partnership for an Advanced Computing Environment (PACE) through its Hive (U.S. National Science Foundation through grant MRI-1828187) and Phoenix clusters at Georgia Institute of Technology, Atlanta, Georgia. P.S. acknowledges discussions with Igor I. Mazin regarding the theoretical underpinnings of orbital-free and Kohn-Sham DFT.

Appendix A: Stress tensor in the Δ -machine learning model

In the Δ -machine learning model, the correction to the stress tensor computed by orbital-free DFT takes the form:

$$\begin{aligned} \sigma_{\Delta,\lambda\mu} &= \frac{1}{V} \left. \frac{\partial E_{\Delta}^F}{\partial F_{\lambda\mu}} \right|_{\mathbf{F}=\mathbf{I}}, \\ &= -\frac{1}{V} \sum_{e=1}^{N_e} \sum_{i=1}^{N_A^e} \sum_{t=1}^{N_T^e} \tilde{w}_i^e \zeta^e k(\mathbf{x}_i^e, \tilde{\mathbf{x}}_t^e) \mathbf{z}_{i,t}^e \cdot \left. \frac{\partial \mathbf{x}_i^e}{\partial F_{\lambda\mu}} \right|_{\mathbf{F}=\mathbf{I}}. \quad (\text{A1}) \end{aligned}$$

where

$$\left. \frac{\partial [\mathbf{x}_i^{eF}]_{n_1 n_2 l}^{e_1 e_2}}{\partial F_{\lambda \mu}} \right|_{\mathbf{F}=\mathbf{I}} = c_l \sum_{m=-l}^l \left(\frac{\partial c_{i, e_1, n_1 l m}^{eF}}{\partial F_{\lambda \mu}} c_{i, e_2, n_2 l m}^{e*F} + c_{i, e_1, n_1 l m}^{eF} \frac{\partial c_{i, e_2, n_2 l m}^{e*F}}{\partial F_{\lambda \mu}} \right) \Big|_{\mathbf{F}=\mathbf{I}}, \quad (\text{A2})$$

with

$$\left. \frac{\partial c_{i, \tilde{\epsilon}, n l m}^{eF}}{\partial F_{\lambda \mu}} \right|_{\mathbf{F}=\mathbf{I}} = \sum_{j=1}^{N_A^e} \frac{(r_{j\lambda}^{\tilde{e}} - r_{i\lambda}^e)(r_{j\mu}^{\tilde{e}} - r_{i\mu}^e)}{|\mathbf{r}_j^{\tilde{e}} - \mathbf{r}_i^e|} h'_{nl}(|\mathbf{r}_j^{\tilde{e}} - \mathbf{r}_i^e|) Y_{lm}^*(\mathbf{r}_j^{\tilde{e}} - \mathbf{r}_i^e) + h_{nl}(|\mathbf{r}_j^{\tilde{e}} - \mathbf{r}_i^e|) \frac{\partial Y_{lm}^*(\mathbf{r}_j^{\tilde{e}} - \mathbf{r}_i^e)}{\partial (\mathbf{r}_j^{\tilde{e}} - \mathbf{r}_i^e)} \cdot \mathbf{J}^{\lambda \mu}(\mathbf{r}_j^{\tilde{e}} - \mathbf{r}_i^e). \quad (\text{A3})$$

Above, V is the volume of the simulation cell, $F_{\lambda \mu}$ are the Cartesian components of the deformation gradient tensor \mathbf{F} , $(\cdot)^F$ denotes the quantities after deformation, and $\mathbf{J}^{\lambda \mu} \in \mathbb{R}^{3 \times 3}$ denote the single-entry matrices that have a value of 1 at the (λ, μ) position and zeros elsewhere.

DATA AVAILABILITY STATEMENT

The data that support the findings of this study are available within the article and from the corresponding author upon reasonable request.

REFERENCES

- ¹W. Kohn and L. J. Sham, *Physical Review* **140**, A1133 (1965).
- ²P. Hohenberg and W. Kohn, *Physical Review* **136**, B864 (1964).
- ³K. Burke, *The Journal of Chemical Physics* **136** (2012).
- ⁴V. L. Lignères and E. A. Carter, in *Handbook of Materials Modeling: Methods* (Springer, 2005) pp. 137–148.
- ⁵M. Levy, J. P. Perdew, and V. Sahni, *Physical Review A* **30**, 2745 (1984).
- ⁶K. Jiang and M. Pavanello, *Physical Review B* **103**, 245102 (2021).
- ⁷L. H. Thomas, in *Mathematical Proceedings of the Cambridge Philosophical Society*, Vol. 23 (Cambridge University Press, 1927) pp. 542–548.
- ⁸E. Fermi, *Zeitschrift für Physik* **48**, 73 (1928).
- ⁹C. v. Weizsäcker, *Zeitschrift für Physik* **96**, 431 (1935).
- ¹⁰L. A. Constantin, E. Fabiano, and F. Della Sala, *Journal of Chemical Theory and Computation* **15**, 3044 (2019).
- ¹¹K. Luo, V. V. Karasiev, and S. Trickey, *Physical Review B* **98**, 041111 (2018).
- ¹²L. A. Constantin, E. Fabiano, and F. Della Sala, *The Journal of Physical Chemistry Letters* **9**, 4385 (2018).
- ¹³H. I. Francisco, J. Carmona-Espíndola, and J. L. Gázquez, *The Journal of Chemical Physics* **154** (2021).
- ¹⁴J. P. Perdew and L. A. Constantin, *Physical Review B* **75**, 155109 (2007).
- ¹⁵L. A. Constantin, E. Fabiano, and F. Della Sala, *Journal of Chemical Theory and Computation* **13**, 4228 (2017).
- ¹⁶C. Huang and E. A. Carter, *Physical Review B* **81**, 045206 (2010).
- ¹⁷L. A. Constantin, E. Fabiano, and F. Della Sala, *Physical Review B* **97**, 205137 (2018).
- ¹⁸G. S. Ho, V. L. Lignères, and E. A. Carter, *Physical Review B* **78**, 045105 (2008).
- ¹⁹V. V. Karasiev and S. B. Trickey, *Computer Physics Communications* **183**, 2519 (2012).
- ²⁰E. Chacón, J. Alvarillos, and P. Tarazona, *Physical Review B* **32**, 7868 (1985).
- ²¹I. Mazin, *Soviet Physics—Lebedev Institute Reports (English Translation of Sbornik Kratkie Soobshcheniya po Fizike. AN SSSR. Fizicheskii Institut im. P.N. Lebedeva)*, 17 (1988).
- ²²L.-W. Wang and M. P. Teter, *Physical Review B* **45**, 13196 (1992).
- ²³Y. A. Wang, N. Govind, and E. A. Carter, *Physical Review B* **60**, 16350 (1999).
- ²⁴K. M. Carling and E. A. Carter, *Modelling and Simulation in Materials Science and Engineering* **11**, 339 (2003).
- ²⁵B. Zhou, V. L. Lignères, and E. A. Carter, *The Journal of Chemical Physics* **122** (2005).
- ²⁶G. Ho, M. T. Ong, K. J. Caspersen, and E. A. Carter, *Physical Chemistry Chemical Physics* **9**, 4951 (2007).
- ²⁷I. Mazin and D. Singh, *Physical Review B* **57**, 6879 (1998).
- ²⁸X. Shao, W. Mi, and M. Pavanello, *Physical Review B* **104**, 045118 (2021).
- ²⁹W. Mi, A. Genova, and M. Pavanello, *The Journal of Chemical Physics* **148** (2018).
- ³⁰Q. Xu, C. Ma, W. Mi, Y. Wang, and Y. Ma, *Nature Communications* **13**, 1385 (2022).
- ³¹I. Shin and E. A. Carter, *The Journal of Chemical Physics* **140** (2014).
- ³²P. Golub and S. Manzhos, *Physical Chemistry Chemical Physics* **21**, 378 (2019).
- ³³M. Alghadeer, A. Al-Aswad, and F. H. Alharbi, *Physics Letters A* **414**, 127621 (2021).
- ³⁴M. Fujinami, R. Kageyama, J. Seino, Y. Ikabata, and H. Nakai, *Chemical Physics Letters* **748**, 137358 (2020).
- ³⁵P. del Mazo-Sevillano and J. Hermann, *arXiv preprint arXiv:2306.17587* (2023).
- ³⁶R. Remme, T. Kaczun, M. Scheurer, A. Dreuw, and F. A. Hamprecht, *arXiv preprint arXiv:2305.13316* (2023).
- ³⁷K. Ryczko, S. J. Wetzel, R. G. Melko, and I. Tamblyn, *Journal of Chemical Theory and Computation* **18**, 1122 (2022).
- ³⁸S. Kumar, B. Sadigh, S. Zhu, P. Suryanarayana, S. Hamel, B. Gallagher, V. Bulatov, J. Klepeis, and A. Samanta, *The Journal of Chemical Physics* **156** (2022).
- ³⁹R. Meyer, M. Weichselbaum, and A. W. Hauser, *Journal of Chemical Theory and Computation* **16**, 5685 (2020).
- ⁴⁰J. C. Snyder, M. Rupp, K. Hansen, L. Blooston, K.-R. Müller, and K. Burke, *The Journal of Chemical Physics* **139** (2013).
- ⁴¹G. R. Schleder, A. C. Padilha, C. M. Acosta, M. Costa, and A. Fazzio, *Journal of Physics: Materials* **2**, 032001 (2019).
- ⁴²I. Poltavsky and A. Tkatchenko, *The Journal of Physical Chemistry Letters* **12**, 6551 (2021).
- ⁴³O. T. Unke, S. Chmiela, H. E. Sauceda, M. Gastegger, I. Poltavsky, K. T. Schütt, A. Tkatchenko, and K.-R. Müller, *Chemical Reviews* **121**, 10142 (2021).
- ⁴⁴J. M. Bowman, C. Qu, R. Conte, A. Nandi, P. L. Houston, and Q. Yu, *Journal of Chemical Theory and Computation* **19**, 1 (2022).
- ⁴⁵M. Bogojeski, L. Vogt-Maranto, M. E. Tuckerman, K.-R. Müller, and K. Burke, *Nature Communications* **11**, 5223 (2020).
- ⁴⁶A. Nandi, C. Qu, P. L. Houston, R. Conte, and J. M. Bowman, *The Journal of Chemical Physics* **154** (2021).
- ⁴⁷C. Qu, P. L. Houston, R. Conte, A. Nandi, and J. M. Bowman, *The Journal of Physical Chemistry Letters* **12**, 4902 (2021).
- ⁴⁸P. Zaspel, B. Huang, H. Harbrecht, and O. A. von Lilienfeld, *Journal of Chemical Theory and Computation* **15**, 1546 (2019).
- ⁴⁹R. Ramakrishnan, P. O. Dral, M. Rupp, and O. A. Von Lilienfeld, *Journal of Chemical Theory and Computation* **11**, 2087 (2015).
- ⁵⁰Z. Qiao, M. Welborn, A. Anandkumar, F. R. Manby, and T. F. Miller, *The Journal of Chemical Physics* **153** (2020).
- ⁵¹P. Liu, C. Verdi, F. Karsai, and G. Kresse, *Physical Review B* **105**, L060102 (2022).
- ⁵²C. Verdi, L. Ranalli, C. Franchini, and G. Kresse, *Physical Review Materials* **7**, L030801 (2023).
- ⁵³C. Qu, Q. Yu, R. Conte, P. L. Houston, A. Nandi, and J. M. Bowman, *Digital Discovery* **1**, 658 (2022).
- ⁵⁴C. Qu, Q. Yu, P. Houston, R. Conte, A. Nandi, and J. Bowman, *Preprint, available at Research Square [https://doi.org/10.21203/rs.3.rs-1847384/v1]* (2022).

- ⁵⁵Q. Yu, C. Qu, P. L. Houston, A. Nandi, P. Pandey, R. Conte, and J. M. Bowman, *The Journal of Physical Chemistry Letters* **14**, 8077 (2023).
- ⁵⁶B. Thapa, X. Jing, J. E. Pask, P. Suryanarayana, and I. I. Mazin, *The Journal of Chemical Physics* **158** (2023).
- ⁵⁷A. P. Bartók, M. C. Payne, R. Kondor, and G. Csányi, *Physical Review Letters* **104**, 136403 (2010).
- ⁵⁸A. P. Bartók, R. Kondor, and G. Csányi, *Physical Review B* **87**, 184115 (2013).
- ⁵⁹J. Behler and M. Parrinello, *Physical Review Letters* **98**, 146401 (2007).
- ⁶⁰K. Kaufmann and W. Baumeister, *Journal of Physics B: Atomic, Molecular and Optical Physics* **22**, 1 (1989).
- ⁶¹R. Jinnouchi, F. Karsai, and G. Kresse, *Physical Review B* **100**, 014105 (2019).
- ⁶²C. M. Bishop and N. M. Nasrabadi, *Pattern recognition and machine learning*, Vol. 4 (Springer, 2006).
- ⁶³S. Ghosh and P. Suryanarayana, *Computer Physics Communications* **212**, 189 (2017).
- ⁶⁴S. Ghosh and P. Suryanarayana, *Computer Physics Communications* **216**, 109 (2017).
- ⁶⁵Q. Xu, A. Sharma, B. Comer, H. Huang, E. Chow, A. J. Medford, J. E. Pask, and P. Suryanarayana, *SoftwareX* **15**, 100709 (2021).
- ⁶⁶B. Zhang, X. Jing, Q. Xu, S. Kumar, A. Sharma, L. Erlandson, S. J. Sahoo, E. Chow, A. J. Medford, J. E. Pask, *et al.*, arXiv preprint arXiv:2305.07679 (2023).
- ⁶⁷V. Briganti and A. Lunghi, arXiv preprint arXiv:2303.16538 (2023).
- ⁶⁸T. A. Young, T. Johnston-Wood, V. L. Deringer, and F. Duarte, *Chemical Science* **12**, 10944 (2021).
- ⁶⁹P. Minary, G. J. Martyna, and M. E. Tuckerman, *The Journal of Chemical Physics* **118**, 2510 (2003).
- ⁷⁰D. Hamann, *Physical Review B* **88**, 085117 (2013).
- ⁷¹M. F. Shojaei, J. E. Pask, A. J. Medford, and P. Suryanarayana, *Computer Physics Communications* **283**, 108594 (2023).
- ⁷²J. P. Perdew and A. Zunger, *Physical Review B* **23**, 5048 (1981).
- ⁷³J. P. Perdew, K. Burke, and M. Ernzerhof, *Physical Review Letters* **77**, 3865 (1996).
- ⁷⁴S. Ghosh and P. Suryanarayana, *Journal of Computational Physics* **307**, 634 (2016).
- ⁷⁵P. Suryanarayana and D. Phanish, *Journal of Computational Physics* **275**, 524 (2014).
- ⁷⁶C. Werzsticxer, *Z. Physik* **96**, 431 (1935).
- ⁷⁷B. Zhou, Y. A. Wang, and E. A. Carter, *Physical Review B* **69**, 125109 (2004).
- ⁷⁸Y. Tomishima and K. Yonei, *Journal of the Physical Society of Japan* **21**, 142 (1966).
- ⁷⁹U. Dahlborg, M. Besser, M. Calvo-Dahlborg, G. Cuello, C. Dewhurst, M. J. Kramer, J. R. Morris, and D. Sordelet, *Journal of Non-Crystalline Solids* **353**, 3005 (2007).
- ⁸⁰K. Khoo, T.-L. Chan, M. Kim, and J. R. Chelikowsky, *Physical Review B* **84**, 214203 (2011).
- ⁸¹X. Huang, X. Dong, L. Liu, and P. Li, *Journal of Non-Crystalline Solids* **503**, 182 (2019).
- ⁸²A. Sharma, A. Metere, P. Suryanarayana, L. Erlandson, E. Chow, and J. E. Pask, *The Journal of Chemical Physics* **158** (2023).